

**A Comparison of Terrestrial Laser Scanning and Structure-from-Motion  
Photogrammetry as Methods for Digital Outcrop Acquisition**

*M.W. Wilkinson<sup>1</sup>, R.R. Jones<sup>1</sup>, C.E. Woods<sup>1</sup>, S.R. Gilment<sup>1</sup>, K.J.W. McCaffrey<sup>2</sup>, S. Kokkalas<sup>3</sup>  
and J.J. Long<sup>1</sup>.*

Terrestrial laser scanning (TLS) has been used extensively in Earth Science for acquisition of digital outcrop data over the past decade. Structure-from-Motion photogrammetry (SfM) has recently emerged as an alternative and competing technology. The real-world performance of these technologies for ground-based digital outcrop acquisition is assessed using outcrops from north east England and the United Arab Emirates. Both TLS and SfM are viable methods, although no single technology is universally best suited to all situations. There are a range of practical considerations and operating conditions where each method has clear advantages. In comparison to TLS, SfM benefits from being lighter, more compact, cheaper, more easily replaced and repaired, with lower power requirements. TLS in comparison to SfM provides intrinsically validated data and more robust data acquisition in a wide range of operating conditions. Data post-processing is also swifter. The SfM data sets were found to contain systematic inaccuracies when compared to their TLS counterparts. These inaccuracies are related to the triangulation approach of the SfM method which is distinct from the time-of-flight principle employed by TLS. An elaborate approach is required for SfM to produce comparable results to TLS under most circumstances.

<sup>1</sup>Geospatial Research Ltd, Department of Earth Sciences, Durham University, Durham, DH1 3LE, U.K.

<sup>2</sup>Department of Earth Sciences, Durham University, Durham, DH1 3LE, U.K.

<sup>3</sup>The Petroleum Institute, Petroleum Geoscience Department, P.O. Box 2533, Abu Dhabi, U.A.E.

## 1. INTRODUCTION

Digital outcrop acquisition is the process of obtaining a digital representation of an outcrop with sufficient detail, precision and accuracy such that it forms a usable duplication of its real-world counterpart, most commonly presented as a three-dimensional model (Xu et al., 2000; Pringle et al., 2001; Jones et al., 2004, 2009; Bellian et al., 2005, Clegg et al., 2005; Hodgetts et al., 2004). Digital outcrop models provide a means to gain quantitative data (e.g. Ahlgren et al., 2002; Trinks et al., 2005; McCaffrey et al., 2005; Jones et al., 2008a; Enge et al., 2010) over a range of scales, forming a key input in reservoir geomodeling workflows (Pringle et al., 2004, 2006; Thurmond et al., 2006; Labourdette and Jones, 2007; Howell et al., 2014).

No single technology is universally best suited to all digital outcrop acquisition. Successful acquisition relies on three interrelated factors: (1) An understanding of the range of acquisition methods available, and their application; (2) selection of one or more suitable methods for a chosen outcrop; and (3) the required geological measurements and interpretations to be made from the digital representation. In many cases there are limitations in the available acquisition methods and/or suitable outcrops at which to apply these successfully, thus forcing compromise of the all-important measurements and interpretations. Skill with multiple acquisition methods and an appreciation of their strengths and weaknesses are therefore vital to acquire suitable data for any given outcrop and purpose.

A range of different digital outcrop acquisition methods exist: these methods can be split into airborne and ground-based approaches. Airborne methods and applications include the use of airborne laser scanning from conventional aircraft; for example, as used to analyse faulting in Slovenia (Cunningham et al., 2006), and the San Andreas fault (Bevis, et al., 2005; Arrowsmith and Zielke, 2009; Hilley et al., 2010) and to model paleokarst layers in the

Billefjorden region of Svalbard (Buckley et al., 2008a); unmanned aerial vehicle (UAV) mounted laser scanning (Lin et al., 2011) and Structure-from-Motion (SfM) photogrammetry, as used to map coastal erosion (Mancini et al., 2013); SfM photogrammetry from manned aircraft, as used to monitor active lava dome topography (James and Varley, 2012); and kite-mounted SfM photogrammetry, as used, for example, to construct multispectral terrain models of intertidal landscapes at Greenfields beach, New South Wales (Bryson et al., 2013).

Ground based methods of outcrop acquisition are used in a very wide range of diverse applications. Examples include: (1) terrestrial laser scanning (TLS), used to characterise fracture systems (Ahlgren et al., 2002), to map Miocene deep-water slope-channel architecture in Victorio Canyon, West Texas (Bellian et al., 2005), to analyse fluvial channel architectures near Ainsa, Spain (Labourdette and Jones, 2007), and to describe dolomite bodies, in three dimensions, within the Latemar platform carbonates, in northern Italy (Jacquemyn et al., 2015); (2) standard stereo-pair photogrammetry used to analyse Carboniferous marine sequences (Pringle et al., 2004), (3) structure-from-motion (SfM) photogrammetry, used to measure structural features in folded Upper-Cretaceous marl and limestone, in southwest Vienna (Schober and Exner, 2011); (4) real-time kinematic global positioning systems (GPS), used to quantify fold geometries in Carboniferous limestones in NE England (Pearce et al., 2006); (5) combined GPS and laser range finding, used to map synsedimentary growth faults at Muddy Creek, Wyoming (Xu et al., 2000); and (6) time-of-flight camera range imaging that was used to analyse speleothem features at short range in Dechen Cave near Dortmund, Germany (Hammerle et al., 2014).

Hybrid approaches combining air and ground based methods have also been implemented (e.g. Pringle et al., 2004; Jones et al., 2009; Buckley et al., 2010; Bemis et al., 2014; Jacquemyn et al., 2015). Overhanging and vertically orientated outcrop can be

problematic to acquire from an aerial perspective. Combining ground and aerial methods helps to address this issue. Methods to extend virtual outcrop models into the shallow subsurface are summarised in Pringle et al., (2006) and Jones et al., (2011).

Of all the ground-based methods TLS and SfM provide the most comprehensive and versatile outcrop representations, at scales where measurements were traditionally taken directly by hand at the outcrop. Most published studies are based on either TLS or SfM, although both methods can be combined as hybrid data sets in order to maximise spatial coverage and point density, for instance during topographic mapping of the Fogo volcano following the 2014-2015 eruption (Richter et al., 2016).

The aim of this study is to provide a robust comparative analysis of the real-world performance of these two methods using corresponding data acquired at outcrops in north east England and the United Arab Emirates. SfM is often presented as a simpler and cheaper alternative to TLS: however comparison of the two methods shows strengths and weaknesses in both and reveals subtle but significant differences in their output. Our comparison provides an indication of the elaborate approach required for the successful implementation of SfM. The advantages and limitations of the two methods from our experience will also be discussed, including important practical considerations for field-based geoscientists.

## **2. ACQUISITION METHOD OVERVIEW**

### **2.1. Terrestrial Laser Scanning**

Over the past decade terrestrial laser scanning (TLS) has been used extensively in Earth Science as a tool for acquisition of three-dimensional outcrop surface data sets (Jones et al., 2008b). The technology, its performance and its application for common acquisition tasks and analyses within Earth Science are well established (Slob and Hack, 2004, Buckley et al., 2008b, Heritage and Large, 2009). Laser emissions are confined to the near-infrared to

ultraviolet spectrum. These electromagnetic waves do not travel through solid objects; this, to acquire data the laser scanner must have a direct unobstructed line of sight to the outcrop of interest. Many outcrops are geometrically complex and cannot usually be seen in their entirety from a single vantage point. This self-obstruction leads to shadow regions within the laser scan data, which are minimised by placing the laser scanner in a number of vantage points (often termed scan positions) about the outcrop. Point clouds generated from different scan positions are typically co-located using reflective targets which act as common reference points to align multiple point clouds within a common co-ordinate system. The process of aligning multiple scan positions to a georeferenced reflector array also provides an independent validation of the accuracy of the laser scanner. The real-world positions of reflectors are commonly measured using the Global Navigation Satellite System (GNSS). The areas of the scanned outcrops are sufficiently small for the curvature of the earth to be ignored. Comparison of the scan-based and real-world reflector positions are then used to generate a transformation matrix describing the rotation and translation required to align the reflectors and scan data to real-world positions (Table S1). Scaling is unaltered in this process and is calculated independently at the time of acquisition using calibration parameters relating the laser wave velocity in air of known temperature, pressure and humidity.

The flexibility of this TLS technology provides a potentially vast range of applications beyond outcrop acquisition and feature mapping. Applications include temporal change detection (Alba and Scaioni, 2010, Abellán et al., 2011, Lim et al., 2011, Wilkinson et al., 2010, 2012, DeLong et al., 2014) and the integration with other acquisition techniques such as multispectral imagery (Buckley et al., 2013) and ground penetrating radar (Jones et al., 2011, Bubeck et al., 2015).

## 2.2. Structure-from-Motion Photogrammetry

Structure-from-motion (SfM) photogrammetry involves the three-dimensional reconstruction of a scene from a suite of two-dimensional images (Ullman 1979). The Structure-from-Motion photogrammetry acquisition and subsequent image processing workflow have been previously described in numerous different implementations and adaptations (e.g. James and Robson, 2012, 2014, Westoby et al., 2012, Bemis et al., 2014). Acquisition involves the collection of a suite of overlapping digital images of the outcrop from multiple perspectives. Each piece of outcrop must be seen in at least two images in order for the processing workflow to successfully reconstruct its three-dimensional geometry, although in practice the outcrop is imaged to a greater degree in order to provide additional redundancy. Differing perspectives between multiple images sampling the same piece of outcrop are maximised, whilst maintaining significant similarity between images in order to constrain the geometric reconstruction from multiple orientations. The concept of achievable precision is explored in detail by James and Robson (2012) who identify a number of parameters that affect reconstruction. Parameters include the strength of the photogrammetric network, the mean distance from camera to the outcrop, the number of overlapping images, and parameters relating to the intrinsic and extrinsic properties of the camera body and lens in use, such as sensor size and parameters describing focal length and lens distortion. Acquiring multiple images of each piece of the outcrop from sufficiently different ground-based perspectives presents a challenge, even when several vantage points exist. Multi-rotor unmanned aerial vehicles (UAVs) provide a solution through their ability to hover and image the outcrop from a greater range of perspectives (e.g. Bemis et al., 2014). Following image acquisition the three-dimensional digital outcrop model is produced by processing the images on a workstation using a photogrammetric workflow (e.g. Figure 1). Success of the SfM approach relies on the ability of the workflow to detect and match correspondingly distinct

outcrop features (often termed key points) between images. The scale-invariant feature transform (SIFT) (Lowe, 2004) is a common implementation of feature detection and matching. Each key point identified in multiple images is included in the final outcrop model as a discrete point in 3D space, providing it passes a set of quality assessment criteria (commonly a minimum and maximum perspective change between the seed images and its position conformance with surrounding key points). A camera calibration model (e.g. Brown, 1966) describing the radial, tangential and decentering distortion of the image due to lens and camera body is used to remove these effects by undistorting the images prior to key point detection and matching (Figure 1, step A). If the camera calibration is unknown, an estimate can be calculated during the matching process, although the final accuracy of the outcrop model will be compromised. Key point detection and matching are then applied to the image suite (Figure 1, steps B and C). The distribution of matches between images and how this array changes between images are used to calculate the relative position and orientation of each image in 3-D space (Figure 1, step D). Once the camera positions and orientations are known, the matches can be projected to form a sparse point cloud outcrop model (Fig. 1, step E), and the result can be visualised. Images with poor similarity to others in the suite do not contain enough valid matches to calculate their position and orientation within the model and thus are excluded from the rest of the workflow. Excluded images can disrupt outcrop reconstruction, particularly if image acquisition was conducted in a simple chain-like manner where little overlap exists in the images beyond their immediate neighbours. To increase outcrop model point density the workflow interrogates the images used in the sparse model with increased aggressiveness in the search for further key point matches (Fig. 1, step F). This is computationally intensive but the comparison of images is limited to those that are known to overlap by using the image positions and orientations calculated during the generation of the sparse model. The dense outcrop model is presented in its own

photogrammetric co-ordinate system which lacks real-world scale, orientation and position. Reference data are used to scale, orientate and position the outcrop model into a real-world co-ordinate system (Table S2). Reference data exist in a range of precisions and accuracies that provide solutions of varying quality. Such data include outcrop control points surveyed using GNSS, vertically orientated surveyor's poles of known length, as well as the position and orientation of the camera measured at the time of image acquisition (for an evaluation of referencing methods see Sturzenegger and Stead, 2009). A transformation matrix is calculated by comparing the reference data with their counterpart representation in the photogrammetric coordinate system. The matrix is used to transform the dense outcrop model from photogrammetric to real-world co-ordinate systems. The transformation forms the final stage of the SfM workflow (Fig. 1, step G), after which the outcrop model is ready for further task-specific processing and interpretation.

### **3. OUTCROP DATA SETS**

Two outcrops representing typical study sites were chosen for a real-world comparison of the two acquisition methods: a Carboniferous limestone quarry outcrop in north east England and a fractured Cretaceous limestone outcrop near Ras al-Khaimah, United Arab Emirates. Both outcrops were selected for their geological interest, specifically the three-dimensional exposure of fracture surfaces, rather than their particular suitability to either method. The data were acquired and processed using a range of field equipment and software, in the manner described in Section 2. An overview of the acquisition parameters and summary output for each method at both study sites is given in Table 1.

#### **3.1. Limestone Quarry, North East England**

A disused quarry near Stanhope in north east England ( $54.7104^{\circ}$ ,  $-002.024^{\circ}$ ) was selected as the first site for this comparative study (Figs. 2A and B). The quarry exposes a 10

m high north facing vertical wall of fractured Carboniferous limestone along a 260 m east-west cut. The outcrop is similar in extent and access to a classical road cut exposure. Material has been extracted from the quarry through exploitation of the bedding-perpendicular natural fracture network, by prying naturally formed blocks from the face. The outcrop surface is therefore complex and angular, formed from a series of semi-planar faces representing fracture surfaces. A 20-m-wide quarry floor exists at the base of the outcrop, beyond which the surrounding hillsides to the north and northeast provide natural vantage points from which to observe the outcrop.

### ***3.1.1. Terrestrial Laser Scan Data Set***

The TLS data set was acquired over a four hour period in overcast conditions. A Leica ScanStation C10 TLS (Fig. 3A) was used to acquire data at ranges of between 20 and 50 meters from four scan positions (Fig. 2B), which provided near-complete data capture with minimal shadow. The Leica ScanStation C10 uses a visible green laser to acquire measurements with 6 mm accuracy ( $1\sigma$ ) in standard conditions up to 50 m range (Leica Geosystems, 2011), of which the 0 - 50 m range encompasses the majority of the data acquired in this survey. Images acquired with a 4 megapixel digital camera internal to the scanner were used to colour the point data to provide a visually accurate representation of the outcrop; their use is aesthetic only and does not influence the geometry of the resultant model. The vertical axis of each scan data set was constrained using the scanner's dual axis compensator with 1.5 arcsecond accuracy. Constraining the vertical axis simplifies the remaining alignment to rotations about this axis and translations within a Cartesian coordinate system. Three retroreflective targets (Figs. 2B and 3B) surrounding the outcrop were used to align the four scan positions into a single model. The targets were surveyed using GNSS. The GNSS data were post-processed relative to a local base station to provide reflector positions with centimetre accuracy. These GNSS-derived positions were used to

transform the scan model into a real-world co-ordinate system (Table S1). Following transformation the outcrop model was cropped to remove points outside of the exposed area of interest, such as the surrounding hillsides, vegetation and the quarry floor. The resultant final outcrop model (Fig. 3C) contains 1.79 million points, with an average density of 1710 points per m<sup>2</sup> and an average point spacing of 0.02 m.

### ***3.1.2. Structure-from-Motion Photogrammetric Data Set***

The SfM data set was acquired over a two hour period in overcast conditions. The requirement to produce a model with point spacing comparable to the TLS data set was considered during selection of camera equipment and appropriate distance to the outcrop. A 12 megapixel Nikon D300 with Nikon AF-S DX Nikkor 10-24 mm f/3.5-4.5G ED and Nikon AF-S DX Nikkor 55-200 mm f/4.5-5.6G IF-ED VR lenses were used to acquire 200 images from 11 different vantage points (Fig. 4A). The focal lengths of the zoom lenses were taped fixed at 24 mm and 125 mm, respectively. Three of the vantage points were located within 10 – 30 m of the outcrop from which the 24 mm lens was used. The remaining eight vantage points were located within 200 – 250 m of the outcrop and images were acquired using the 125 mm lens. The images from the 11 vantage points covered the extent of the outcrop with sufficient overlap and similarity to enable SfM reconstruction. Of the 200 images, 44 were acquired from four tripod positions, representing four of the 11 vantage points (Figs. 2B and 4B). A Trimble 5800 GPS receiver was set up as a local base station to record pseudorange and position data at one-second intervals for the entirety of the survey. A Spectra Precision ProMark 120 GNSS receiver occupied each tripod position for 30 minutes and recorded GNSS data at one-second intervals. Baselines between the base station and each tripod position were post-processed using Trimble Geomatics Office software to provide tripod positions with centimetre accuracy relative to the base station. The SfM processing workflow described in Section 2.2 was implemented using the visualSFM software package version

0.5.26 (Wu, 2007, 2013, Wu et al., 2011) to create the outcrop model. A PC workstation with dual Xeon E5-2620 processors and 128 GB RAM was used for this purpose due to its multithreading capability of 24 threads at 2.0 Ghz. The 24 mm and 125 mm lenses were calibrated using Agisoft Lens software version 0.4.1 to provide radial, tangential and decentering distortion coefficients. The images were undistorted using this calibration prior to use in the SfM workflow (e.g. Fig. 4C). Key-point detection and matching aligned all 200 photos into a single photogrammetric model, providing a sparse point cloud and the orientations and relative positions of the cameras (Fig. 4B). A dense point cloud was subsequently computed by allowing the SfM software to produce the most detailed data set possible. The resultant data set contains 0.96 million points, with an average density of 880 points per m<sup>2</sup> and an average point spacing of 0.03 m. The outcrop model was converted into a real-world reference frame by calculating the transformation matrix between the four tripod positions within the photogrammetric reference frame and their GNSS-derived positions in real-world co-ordinates (Fig. 4D). A summary of this transformation is shown in Table S2.

### **3.2. Ras al-Khaimah, United Arab Emirates**

Data for the second comparative study were acquired from a wadi outcrop (25.947°, 056.072°) near Ras al-Khaimah, United Arab Emirates (Figs. 5A and 5B). The east-west trending outcrop extends 250 m up the wadi and exposes a 45 m high south facing terraced slope, comprised of well-bedded and well-fractured Cretaceous limestone (Wasia Group). The outcrop is located in the footwall of a high angle reverse fault that dips towards the east, displacing the older Thamama Group in the hanging wall. Weathering of bed-bound, bedding-perpendicular fractures has resulted in rounded, undulating fracture surfaces. The 40 m wide wadi is accessed by track to the west and is limited in extent to the east by tailings from a nearby quarry.

### ***3.2.1. Terrestrial Laser Scan Data Set***

The TLS data set was acquired over a two-and-a-half hour period in sunny conditions. A Riegl LMS-Z420i TLS (Fig. 6A) was used to acquire data at ranges of between 100 and 200 meters from two scan positions. A Nikon D300 digital camera with 14 mm lens was mounted on the scanner and used to acquire imagery to colour the point cloud data. The Riegl LMS-Z420i uses a near-infrared laser to acquire measurements with 8 mm precision ( $1\sigma$  at 50 m) between ranges of 2 – 1000 m [Riegl Laser Measurement Systems, 2010]. Four cylindrical reflectors (e.g. Fig. 6B) provided common marker points between the two scan positions which allowed them to be aligned within a single internal co-ordinate system. The real-world positions of the cylindrical reflectors were surveyed using GNSS in a base-rover configuration, with the raw data post-processed to provide centimetre accuracy. A transformation matrix was calculated by comparing the reflector positions in the internal co-ordinate system with their real-world GNSS-derived co-ordinates (Table S1) and then applied to the TLS data set to rotate and translate it into real-world co-ordinates. The outcrop model was then cropped to remove points outside of the region of interest. The final model (Fig. 6C) contains 1.40 million points, with an average density of 206 points per  $m^2$  and an average point spacing of 0.07 m.

### ***3.2.2. Structure-from-Motion Photogrammetric Data Set***

The SfM data set was acquired over a two-and-a-half hour period in sunny conditions. The outcrop faced south and was well lit by the sun from behind the camera. The requirement to produce a model with point spacing comparable to that of the TLS data set was considered during selection of camera equipment and appropriate distance to the outcrop. An 18 mega-pixel Canon 650D with Canon EF 24-105 mm f/4.0 L IS USM lens with the focal length taped fixed to 24 mm (Fig. 7A) was used to acquire 337 images at a distance to the outcrop of ca. 60 m. Of these images, 73 were positioned across five tripod positions placed at various

vantage points in front of the outcrop (Figs. 5B and 7B). The remaining images were taken freehand and acted as fill-in between the tripod positions, such that the image suite covered the outcrop extent with sufficient similarity between multiple images. The tripod positions were surveyed using GNSS relative to a local base station in the manner described in Section 3.1.2. The 24 mm lens was calibrated using Agisoft Lens software version 0.4.1 to provide radial, tangential and decentering distortion coefficients. The images were subsequently undistorted using this lens model (Fig. 7C) and loaded into the visualSfM software package version 0.5.26 (Wu, 2007, 2013; Wu et al., 2011) to create the outcrop model. A PC workstation with dual Xeon E5-2620 processors and 128 GB RAM was used for this purpose. Key-point detection and matching aligned all 337 images into one photogrammetric model, providing a sparse point cloud, and identifying the orientation and relative position of the cameras (Fig. 7B). A dense point cloud was subsequently computed by allowing the SfM software to produce the most detailed data set possible. This data set contains 3.36 million points, with an average density of 503 points per  $\text{m}^2$  and an average point spacing of 0.04 m. The outcrop model was scaled, rotated and translated into its real-world position through calculation of a transformation matrix describing the alignment of the five tripod positions from the photogrammetric reference frame to the GNSS-derived real-world co-ordinates (Fig. 7D). A summary of this transformation is shown in Table S2.

#### **4. COMPARISON**

Comparing and assessing point cloud data sets can be a detailed task, because these data are geometrically complex and are often subtly different, due to the way in which different methods sample the outcrop with heterogeneous point spacing and density (e.g. Khoshelham, 2011). A residual point-to-point based comparison using the CloudCompare software version 2.7.0 (EDF R&D, 2015) is presented here, whereby two point clouds (a reference point cloud and a comparison point cloud) are compared by calculating the distance

between every point in the comparison point cloud to the nearest point in the reference point cloud. In order to visualise the difference between the two data sets each point within the comparison cloud is coloured to represent its distance to the nearest reference point (e.g. Figs. 8 and 9). For the point-to-point approach to be effective, the process relies on the residuals between the two point clouds to be of a similar magnitude to their point spacing; the two point clouds must be properly co-located in three-dimensional space, of similar extent and the point clouds must not be too sparse. No feature detection algorithms are applied during this process, it is a simple nearest neighbour calculation to the reference point cloud, whether that is a representation of the same part of the outcrop as the comparison point or not. For the purposes of comparison and validation the terrestrial laser scan data sets were used as the point of reference, this being the most established and directly validated of the two methods (Boehler et al., 2003, Alba and Scaioni, 2007, Buckley et al., 2008b, Reshetyuk, 2009) and generally used as the benchmark case in comparative studies (e.g. Castillo et al., 2012; Favalli et al., 2012; Gómez-Gutiérrez et al., 2014; Nouwakpo et al., 2016).

#### **4.1. Limestone Quarry, North East England**

The precisions reported during the post-processing of the GNSS survey data showed that the position data for the surveyed points from this outcrop were precise to centimetre levels relative to each base station position. The TLS and SfM surveys were conducted on different days about two years apart (7 September 2011 and 21 October 2013, respectively). Two different base station locations were used. As a consequence, the two GNSS surveys with internal centimetre precision are of lower absolute accuracy. Typically the base station locations have decimetre accuracies, and hence the reflector and tripod positions that are georeferenced to them also inherit this accuracy. Any misalignment of the two point clouds in their respective GNSS-derived positions is therefore a composite error that consists of: (1) differences in their absolute position and alignment as determined by the quality of the GNSS

survey data; and (2) any differences in morphology between the two point clouds due to method-dependent acquisition, internal processing factors, or physical changes such as vegetation and rock falls. Therefore a fine-refinement of the alignment of the SfM point cloud was conducted in order to correct for the offset to the TLS point cloud due to the difference in absolute positioning of the GNSS surveys. The refinement was conducted using the iterative closest point (ICP) algorithm (Besl and McKay, 1992) by calculating the transformation required to align the SfM point cloud to the TLS point cloud such that the point-to-point distances are minimised. The process assumes that the two point clouds are already closely aligned such that a correct alignment can be converged upon by minimising the mean of point-to-point distances. The fine-refinement transformation parameters that correct for the offset are shown in Table S2. The fine-refinement process aligned the two point clouds more closely and enabled the point-to-point distance comparison to be implemented in order to investigate differences in the morphology of the point clouds (Fig. 8A). The mean point-to-point distance between the two point clouds was 0.052 m, with a  $1\sigma$  confidence bound of 0.048 m (Fig. 8B and Table 1). Visualisation of point-to-point distances on the SfM point cloud showed mostly consistent point-to-point distances across the outcrop (Fig. 8A). The mean point-to-point distance of 0.052 m is a realistic minimum given the theoretical ground sample distance of 0.004–0.020 m for the photogrammetric images and the average point spacing of 0.02–0.03 m for the two data sets. A relative precision ratio of 1:1563 can be estimated, assuming a mean distance from image to outcrop of 75 m (calculated by assuming images at  $\approx 20$  m distance affect precision more than those at  $\approx 200$  m) and using the standard deviation of point-to-point differences with respect to the TLS data set of 0.048 m as a proxy for local surface standard deviation within the SfM point cloud.

Regions where the point-to-point distances were significantly higher than average are attributed to three factors: (1) Morphological differences between the two point clouds, such

as non-linear distortions that cannot be corrected using a linear transformation applied to the entire outcrop. For example, the ICP alignment converges on the smallest possible overall mean of point-to-point distances, and during this process it accentuated morphological anomalies on east-facing outcrop while minimising it on all others (Figs. 8A and 8C); (2) reduced fidelity (rounding off of sharp edges) within the SfM point cloud with respect to the TLS point cloud (Figs. 8D and 8E); and (3) variation in limited, localised areas due to additional vegetation growing on the outcrop in the interim period between the TLS and SfM surveys (Fig. 8A).

#### **4.2. Ras al-Khaimah, United Arab Emirates**

The SfM and TLS surveys were conducted on the same day (27<sup>th</sup> April, 2015) and shared a common base station position for their GNSS surveys. Post-processing of the GNSS survey data showed that the position data for the SfM tripod positions and TLS reflector positions were accurate to centimetre levels relative to the base station. The use of a shared base station in the SfM and TLS surveys meant that the GNSS-derived alignment of the two data sets was already closely positioned in an absolute sense. Fine refinement of the alignment of the SfM point cloud was conducted using the ICP method described in Section 4.1. The fine-refinement transformation parameters are shown in Table S2 and describe a set of minor rotations and translations that align the SfM point cloud to the TLS point cloud. Following the fine refinement the point-to-point distance comparison was used to investigate differences in the morphology of the point clouds (Fig. 9A). The mean point-to-point distance was 0.074 m with a  $1\sigma$  confidence bound of 0.052 m (Fig. 9B and Table 1). This is a realistic minimum given the theoretical ground sample distance of 0.017 for the photogrammetric images and the average point spacing of 0.04–0.07 m for the SfM and TLS data sets, respectively. A relative precision ratio of 1:1154 can be estimated assuming a mean distance from image to outcrop of 60 m and using the standard deviation of point-to-point differences

with respect to the TLS data set of 0.052 m as a proxy for local surface standard deviation within the SfM point cloud.

Three clear morphological features were revealed in the visualisation: (1) Increased point-to-point distances on many of the vertical outcrop faces (Figs. 9A, 9C and 9D), representing a small lateral offset of the SfM point cloud with respect to its TLS counterpart. This indicates reduced internal consistency within the SfM point cloud, because the ICP algorithm cannot eliminate this effect by homogeneous transformation of the outcrop. (2) Increased point-to-point distances at outcrop edges due to reduced fidelity (rounding off of edges) with respect to the TLS point cloud (Figs. 9A and 9E). This is a good example of how SfM data fidelity can degrade significantly if images lack sufficient contrast and perspective change in order to depict the subtle details of the outcrop; (3) Increased point-to-point distances in limited and localised areas due to poorly constrained points located within vegetation growing on the outcrop (Fig. 9A).

## **5. DISCUSSION**

The direct comparison of the TLS and SfM data sets presented in Section 4 reveals that both methods are generally suitable for the acquisition of outcrop models but that subtle differences in the performance of the two methods exist. The SfM method produced results that are broadly comparable to TLS for the two outcrops, using similar survey design, distance from the outcrop and camera equipment. Of the two outcrop examples presented here the limestone quarry SfM data set is a closer match to its TLS counterpart, however this is mostly due to a lower mean point spacing in both the TLS and SfM data sets for this outcrop. Both SfM examples honoured their TLS counterpart with mean point-to-point distances approaching the mean point spacing for the two data sets (Table 1). Deviation from a consistent match was found to have two distinct causes. Firstly, morphological differences

between the point clouds that could not be eliminated using a single homogeneous transformation caused the most distinct mismatch (Figs. 8C, 9C and 9D). This mismatch suggests that internal inconsistencies exist within the SfM point clouds. These are particularly prevalent when there are restricted perspective differences in the images at the periphery of the survey area due to limited access. Nouwakpo et al., (2016) observed a similar effect with SfM reconstruction of a bare soil surface imaged at  $\approx 2$  m range and attributed this to projective compensation of the SfM workflow due to poor image convergence at the periphery of the survey area.

The second main cause of mismatch in the results is reduced fidelity in the finer details of the SfM point cloud with respect to the TLS point cloud. This mismatch produced characteristic rounding off of the sharp edges of the outcrop (Figs. 8D, 8E, and 9E). This rounding off can be attributed to a lack of small-scale image contrast and perspective change between images within these areas sufficient to reconstruct their true small-scale geometric complexity. This effect could probably be at least partially mitigated by acquiring higher-resolution and lower-noise imagery, using sharp (prime) lenses, optimising camera settings (exposure, focussing and depth of field), and utilising image post-processing to improve contrast, reduce lens artefacts (such as chromatic aberration) and to optimise white-balance.

It is clear from the two comparisons presented here that performance of the SfM method is inconsistent in relation to TLS, and its success is dependent on a multitude of factors that can vary in their individual significance from one outcrop to the next. Indeed, SfM is not a straightforward technique to implement reliably, and there are many factors that affect acquisition and must be considered carefully in order to yield consistent results. Wide variation in performance of the SfM method in different scenarios is common. Relative precision ratios of SfM data sets when compared to their TLS counterparts provide a means

to compare the performance of the SfM method between studies (Table 2). Favalli et al., (2012) acquired TLS and SfM data sets of three outcrops at short range ( $\approx 1$  m) and compared the SfM reconstruction with respect to the TLS counterparts. Westoby et al., (2012) surveyed a  $\approx 80$  m high coastal cliff at  $\approx 15$  m distance and reported SfM differences in relation to TLS in the range of  $\pm 0.1$  m for low-vegetation areas and  $\pm 0.5$  m for those that were heavily vegetated. James and Robson (2012) surveyed a 60 x 3 m coastal cliff at 20 m distance and reported differences between SfM and TLS of less than 0.02 m for most of the cliff face. Nouwakpo et al., (2016) reported a difference between TLS and SfM data sets of vegetated plots of 5 mm at 2 m distance. Relative precision ratios for these outcrop studies were in the range of 1:150 - 2439 which are broadly comparable with results presented here (1:1154 - 1563). Such variations in precision can make the results of the SfM method difficult to apply consistently in a variety of situations, especially for those geoscientists new to the technique.

Typically TLS provides a superior and consistently more robust data set when compared with SfM. In a practical sense the TLS concept of a calibrated time-of-flight device that combines measurements of range and orientation is inherently more robust than the triangulation approach used in SfM. This is not to say that the SfM method is inherently flawed. The main practical drawback of the SfM method is the uncertainty of the internal consistency of the model, in particular an inability to predict the magnitude and extent of non-uniformity (model distortion) within the data. The comparison of TLS time-of-flight measurements to a small number of reflectors whose positions are surveyed using GNSS is sufficient to provide a relatively robust validation of the spatial accuracy of the entire TLS data set (Table S1). In contrast, within the SfM method limited subsets of images (those taken from tripod positions) have their position independently validated with respect to comparable GNSS positions (Table S2). The position of the remaining images and the orientations of the entire image suite are not extrinsically validated, and generally such a limited comparison is

insufficiently robust to validate the internal consistency and spatial precision of the entire data set. The crux of the challenge is threefold: (1) Due to real-world practicalities the ideal image suite required to guarantee consistency and precision can very rarely be consistently acquired in a wide variety of field scenarios (i.e. due to poor outcrop access; lighting conditions, and geometrical outcrop complexity). (2) Previously available off-the-shelf GNSS equipment has not been able to provide sufficiently accurate post-processed positions and orientations for each and every acquired image in an unobtrusive, cost-effective and time-efficient manner. (3) It is generally impractical to survey ground control points (known markers on the outcrop seen in the point cloud model) with sufficient density to validate the entire data set, especially when applied to directly inaccessible outcrops.

There are a number of approaches that could be applied to improve the internal consistency of the SfM surveys in this study. These include the use of prime (i.e. single focal length) lenses, fixing the focussing of the camera lens because the camera calibration is known to vary with focussing (Fryer and Brown, 1986), image correction for chromatic aberration (e.g. Remondino and Fraser, 2006), and the use of additional ground control points to try to provide extra constraint and further independent validation of the models. In order to explicitly constrain the positions and orientations of the entire image suite, next-generation GNSS chipsets and 9-axis inertial measurement units (IMUs) appear to have the potential to offer sufficient functionality to provide high accuracy post-processed data in a compact and cost-efficient package.

These current limitations further highlight the complexity of proper implementation of the SfM method. SfM does have an important place as a field-based data acquisition method, however in most situations where data accuracy, consistency, and reliability are paramount (and where there are no means beyond GNSS surveying to validate the results), TLS is

generally superior and preferable. In comparison with TLS, to acquire spatially consistent, high quality data, SfM requires considerably more skill, survey planning, adherence to theoretical principles, and independent validation. In situations where a minimum spatial precision is required across the outcrop, it is insufficient to state that a SfM data set honours a limited number of independently surveyed positions and that on the whole the data “look correct”; in our experience, this approach will typically fail to identify any significant internal inaccuracies within the data. As usual, the key consideration is to ensure that the inherent precision and accuracy of the method are sufficient for the intended application of the data set.

Beyond the direct comparison of the data and its inherent quality, there is a further set of real-world practical considerations, that relates to the suitability and implementation of each method in the field. These practical considerations are outlined in detail for each method in Table 3 and relate to the baseline performance of the two methods, their physical properties, cost, operator and processing requirements, general availability and ease of servicing or part replacement. A comparison of the two methods in this manner provides a basis for selecting the best approach to suit the particular task at hand. Another set of practical considerations of the relative performance and suitability of the two methods in real-world operating conditions is presented in Table 4.

It is clear from this comparison that both methods have their inherent strengths and weaknesses. The ability to be proficient in multiple acquisition methods provides choice for the geoscientist as to which is the most appropriate method to use in particular circumstances. This choice allows for increased flexibility, increased success rates, and improved measurements and interpretations. In many situations, either TLS or SfM can be used successfully to acquire virtual outcrop data, or can be combined to produce hybrid data sets

(e.g. Bistacchi et al., 2011, Barsanti et al., 2012 and Richter et al., 2016), providing the strengths and weaknesses of the methods are considered and the corresponding impact on the planned measurements and interpretations is understood.

## **6. CONCLUSIONS**

Terrestrial laser scanning (TLS) and Structure-from-Motion (SfM) photogrammetry provide competing and complementary methods of digital outcrop acquisition. Comparisons of the two methods illustrate that in general both are well suited for use in the field. Each method produces broadly comparable results and can be applied successfully in a wide range of situations. The suitability of each method under specific circumstances depends on the purpose of the work, the expected results, the nature of the outcrop, and the prevalent operating conditions.

Real-world considerations in a range of operating conditions highlight the practical strengths and weaknesses of the TLS and SfM methods. SfM equipment is lighter, more compact, cheaper, more easily serviced or replaced, and has lower power requirements. TLS acquisition is more robust (i.e. lower likelihood of inadequate results) in a wider range of operating conditions, is usually extrinsically validated (using GNSS), and data are typically quicker to post-process.

Quantitative comparison of the outcrop models created using both methods indicates that TLS data have higher spatial precision and are more consistent across the outcrop. The fidelity of SfM data is locally reduced due to rounding off (smoothing) of sharp outcrop corners. Spatial precision of SfM data can deteriorate towards the edges of the outcrop, due to poor image convergence towards the periphery of the survey area.

Internal consistency and spatial precision and accuracy are important considerations when using digital outcrop models as the basis for detailed quantitative measurements and

analysis, although these consideration are less important when using virtual outcrops as conceptual analogues or for qualitative studies. Studies based on quantitative analysis of virtual outcrops should include better documentation of spatial error.

## **ACKNOWLEDGEMENTS**

Fieldwork in the United Arab Emirates was carried out with support from Rutherford International Fellowship Program project no. 15312 funded by Petroleum Institute (Abu Dhabi). We thank Alessandro Fornaciai and an anonymous reviewer for constructive and helpful reviews and Francesco Mazzarini for scientific editing.

## REFERENCES CITED

- Abellán, A., Vilaplana, J.M., Calvet, J., García-Sellés, D., and Asensio, E., 2011. Rockfall monitoring by Terrestrial Laser Scanning—Case study of the basaltic rock face at Castellfollit de la Roca (Catalonia, Spain). *Natural Hazards and Earth System Science*, 11(3), 829-841.
- Ahlgren, S., Holmlund, J., Griffiths, P., and Smallshire, R., 2002. Fracture model analysis is simple. *American Association of Petroleum Geologists Explorer*, September 2002.
- Alba, M., and Scaioni, M., 2007. Comparison of techniques for terrestrial laser scanning data georeferencing applied to 3-D modelling of cultural heritage. *The International Archives of the Photogrammetry, Remote Sensing and Spatial Information Sciences*, 36(5/W47), 8.
- Alba, M., and Scaioni, M., 2010. Automatic detection of changes and deformation in rock faces by terrestrial laser scanning: *International Archives of the Photogrammetry, Remote Sensing, and Spatial Information Sciences*, v. 38, Commission V Symposium, p. 11-16.
- Arrowsmith, J.R. and Zielke, O., 2009. Tectonic geomorphology of the San Andreas Fault zone from high resolution topography: An example from the Cholame segment. *Geomorphology*, 113, 70-81.
- Barsanti, S. G., Remondino, F., and Visintini, D., 2012. Photogrammetry and Laser Scanning for archaeological site 3D modelling – Some critical issues: *Proceedings of the Second Workshop on “The New Technologies for Aquileia.”* V. Roberto, L. Fozzati.
- Bellian J.A., Kerans, C., and Jennette, D.C., 2005. Digital Outcrop Models: Applications of Terrestrial Scanning Lidar Technology in Stratigraphic Modeling. *Journal of Sedimentary Research*, 5, 2, 166-176.
- Bemis S.P., Micklethwaite, S., Turner, D., James, M.R., Akciz, S., Thiele, S.T. and Bangash, H.A., 2014. Ground-Based and UAV-Based Photogrammetry: A Multi-Scale High-Resolution Mapping Tool for Structural Geology and Paleoseismology. *Journal of Structural Geology*, 69, 163-178.
- Besl, P.J., and McKay, N.D., 1992. A Method for Registration of 3-D Shapes. *IEEE Trans. on Pattern Analysis and Machine Intelligence* (Los Alamitos, CA, USA: IEEE Computer Society), 14 (2): 239–256.
- Bevis, M., Hudnut, K., Sanchez, R., Toth, C., Grejner-Brzezinska, D., Kendrick, E., Caccamise, D., Raleigh, D., Zhou, H., Shan, S., Shindle, W., Yong, A., Harvey, J., Borsa, A., Ayoub, F., Shrestha, R., Carter, B., Sartori, M., Phillips, D., and Coloma, F., 2005. The B4 project: scanning the San Andreas and San Jacinto fault zones. *American Geophysical Union Fall Meeting*, abstract no. H34B-01.
- Bistacchi, A., Griffith, W.A., Smith, S.A.F., Di Toro, G., Jones, R. and Nielsen, S., 2011. Fault Roughness at Seismogenic Depths from LiDAR and Photogrammetric Analysis. *Pure Applied Geophysics*, 168, 2345-2363.
- Boehler, W., Vicent, M.B., and Marbs, A., 2003. Investigating Laser Scanner Accuracy: Antalya, Turkey, XIX CIPA Symposium, accessed 29/03/2016 from: <https://i3mainz.hs->

mainz.de/sites/default/files/public/data/laserscanner\_accuracy.pdf: International Archives of Photogrammetry, Remote Sensing and Spatial Information Sciences, v. 34, Part 5, p. 696-701.

- Brown, D.C., 1966. Decentering Distortion of Lenses. *Photometric Engineering*, v. 32, no. 3, p. 444-462.
- Bryson, M., Johnson-Roberson, M., Murphy, R.J., and Bongiorno, D., 2013. Kite aerial photography for low-cost, ultra-high spatial resolution multi-spectral mapping of intertidal landscapes. *PloS one*, 8(9), e73550.
- Bubeck, A., Wilkinson, M., Roberts, G.P., Cowie, P.A., McCaffrey, K.J.W., Phillips, R., and Sammonds, P., 2015. The tectonic geomorphology of bedrock scarps on active normal faults in the Italian Apennines mapped using combined ground penetrating radar and terrestrial laser scanning. *Geomorphology*, 237, 38-51.
- Buckley, S.J., Vallet, J., Braathen, A., and Wheeler, W., 2008a. Oblique Helicopter-Based Laser Scanning for Digital Terrain Modelling and Visualisation of Geological Outcrops. *International Archives of the Photogrammetry, Remote Sensing and Spatial Information Sciences*, 37(Part B4).
- Buckley, S.J., Howell, J.A., Enge, H.D., and Kurz, T.H. 2008b. Terrestrial laser scanning in geology: data acquisition, processing and accuracy considerations. *Journal of the Geological Society of London*, 165(3), 625-638.
- Buckley, S.J., Schwarz, E., Terlaky, V., Howell, J.A., and Arnott, R.W.C., 2010. Combining Aerial Photogrammetry and Terrestrial Lidar for Reservoir Analog Modeling. *Photogrammetric Engineering and Remote Sensing*, 76(8): 953-963.
- Buckley, S.J., Kurz, T.H., Howell, J.A., and Schneider, D., 2013. Terrestrial Lidar and Hyperspectral Data Fusion Products for Geological Outcrop Analysis. *Computers and Geosciences*, 54, 249-258.
- Castillo, C., Pérez, R., James, M.R., Quinton, J.N., Taguas, E.V., and Gómez, J.A., 2012. Comparing the Accuracy of Several Field Methods for Measuring Gully Erosion. *Soil Science Society of America Journal*, 76, 1319-1332.
- Clegg, P., Trinks, I., McCaffrey, K.J.W., Holdsworth, R.E., Jones, R.R., Hobbs, R., and Waggott, S., 2005. Towards the Virtual Outcrop. *Geoscientist*, 15(1), 8-9.
- Cunningham, D., Grebby, S., Tansey, K., Gosar, A., and Kastelic, V., 2006. Application of airborne LiDAR to mapping seismogenic faults in forested mountainous terrain, southeastern Alps, Slovenia, *Geophysical Research Letters*, Vol. 33, L20308.
- DeLong, S.B., Pickering, A., Scharer, K.M., Hudnut, K.W., and Lienkaemper, J.J., 2014. Afterslip-Dominated Surface Rupture in the M6.0 South Napa Earthquake as Constrained by Structure-From-Motion Analysis and Terrestrial Laser Scanning. *American Geophysical Union Fall Meeting*.
- EDF R&D, Telecom ParisTech, 2015. CloudCompare (version 2.6.1) [GPL software]. Retrieved from <http://www.cloudcompare.org/>

- Enge, H.D., Howell, J.A., and Buckley, S.J., 2010. Quantifying Clinothem Geometry in a Forced-Regressive River-Dominated Delta, Panther Tongue Member, Utah, USA. *Sedimentology*, 57, 1750-1770.
- Favalli, M., Fornaciai, A., Isola, I., Tarquini, S., and Nannipieri, L., 2012. Multiview 3D reconstruction in geosciences. *Computers & Geosciences*, 44, 168-176.
- Fryer, J.G., and Brown, D.C., 1986. Lens distortion for close-range photogrammetry. *Photogrammetric engineering and remote sensing*, (52), 51-58.
- Gómez-Gutiérrez, Á., de Sanjosé-Blasco, J.J., de Matías-Bejarano, J., and Berenguer-Sempere, F., 2014. Comparing Two Photo-Reconstruction Methods to Produce High Density Point Clouds and DEMs in the Corral del Veleta Rock Glacier (Sierra Nevada, Spain). *Remote Sensing*, 6, 5407-5427.
- Hammerle, M., Hofle, B., Fuchs, J., Schroder-Ritzrau, A., Vollweiler, N., and Frank, N., 2014. Comparison of Kinect and Terrestrial LiDAR Capturing Natural Karst Cave 3-D Objects. *Geoscience and Remote Sensing Letters, IEEE*, 11(11), 1896-1900.
- Heritage, G., and Large, A., 2009. *Laser scanning for the environmental sciences*. John Wiley and Sons.
- Hilley, G.E., DeLong, S., Prentice, C., Blisniuk, K., and Arrowsmith, J.R., 2010. Morphologic dating of fault scarps using airborne laser swath mapping (ALSM) data. *Geophysical Research Letters*, 37, L04301.
- Hodgetts, D., Drinkwater, N.J., Hodgson, D.M., Kavanagh, J., Flint, S., Keogh K.J., and Howell, J., 2004. Three dimensional geological models from outcrop data using digital data collection techniques: an example from the Tanqua Karoo depocentre, South Africa. In Curtis, A. and Wood, R. (Eds) *Geological Prior Knowledge*. Geological Society of London Special Publications, 239, 457-75.
- Howell, J.A., Martinius, A.W., and Good, T.R., 2014. The Application of outcrop analogues in geological modelling: a review, present status and future outlook. Geological Society, London, Special Publications, 387(1), 1-25.
- Jacquemyn, C., Huysmans, M., Hunt, D., Casini, G., and Swennen, R., 2015. Multi-scale three-dimensional distribution of fracture-and igneous intrusion-controlled hydrothermal dolomite from digital outcrop model, Latemar platform, Dolomites, northern Italy. *AAPG Bulletin*, 99(5), 957-984.
- James, M.R., and Robson, S., 2012. Straightforward reconstruction of 3D surfaces and topography with a camera: Accuracy and geoscience application. *Journal of Geophysical Research: Earth Surface* (2003–2012), 117(F3).
- James, M.R., and Robson, S., 2014. Mitigating systematic error in topographic models derived from UAV and ground-based image networks. *Earth Surface Processes and Landforms*, 39, 1413-1420.
- James, M.R., and Varley, N., 2012. Identification of structural controls in an active lava dome with high resolution DEMs: Volcán de Colima, Mexico. *Geophysical Research Letters*, 39(22).

- Jones, R.R., McCaffrey, K.J.W., Wilson, R.W., and Holdsworth, R.E., 2004. Digital field acquisition: Towards increased quantification of uncertainty during geological mapping, in *Geological Prior Information*, edited by A. Curtis and R. Wood, Geol. Soc. Spec. Publ., 239, 43–56.
- Jones, R.R., McCaffrey, K.J.W., Imber, J., Wightman, R., Smith, S.A., Holdsworth, R.E., Clegg, P., De Paola, N., Healy, D., and Wilson, R.W., 2008a. Calibration and validation of reservoir models: the importance of high resolution, quantitative outcrop analogues. Geological Society, London, Special Publications, 309(1), 87-98.
- Jones, R.R., Wawrzyniec, T.F., Holliman, N.S., McCaffrey, K.J.W., Imber, J. and Holdsworth, R.E., 2008b. Describing the dimensionality of geospatial data in the earth sciences – recommendations for nomenclature. *Geosphere*. 4 354-359.
- Jones, R.R., McCaffrey, K.J.W., Clegg, P., Wilson, R.W., Holliman, N.S., Holdsworth, R.E., Imber, J., and Waggott, S., 2009. Integration of regional to outcrop digital data: 3D visualisation of multi-scale geological models. *Computers and Geosciences*, 35(1): 4-18.
- Jones, R.R., Pringle, J.K., McCaffrey, K.J.W., Imber, J., Wightman, R.H., Guo, J. and Long, J.J., 2011. Extending digital outcrop geology into the subsurface. In: Martinsen, O.J., Pulham, A.J., Haughton, P.D.W., Sullivan M.D. (eds) *Outcrops Revitalized - Tools, Techniques and Applications*. *SEPM Concepts in Sedimentology*, 10, 31-50
- Khoshelham, K., 2011 . Accuracy analysis of kinect depth data. In *ISPRS workshop laser scanning* (Vol. 38, No. 5, p. W12).
- Labourdette, R., and Jones, R.R., 2007. Characterization of fluvial architectural elements using a three dimensional outcrop dataset: Escanilla braided system–South-Central Pyrenees, Spain. *Geosphere*, 3, 422–434.
- Leica Geosystems, 2011. ScanStation C10 Product Specifications brochure: [http://hds.leica-geosystems.com/downloads123/hds/hds/ScanStation%20C10/brochures-datasheet/Leica\\_ScanStation\\_C10\\_DS\\_en.pdf](http://hds.leica-geosystems.com/downloads123/hds/hds/ScanStation%20C10/brochures-datasheet/Leica_ScanStation_C10_DS_en.pdf) (04/2016).
- Lim, M., Rosser, N.J., Petley, D.N., and Keen, M., 2011. Quantifying the controls and influence of tide and wave impacts on coastal rock cliff erosion. *Journal of Coastal Research*, 27(1), 46-56.
- Lin, Y., Hyyppä, J., and Jaakkola, A., 2011. Mini-UAV-borne LIDAR for fine-scale mapping. *Geoscience and Remote Sensing Letters, IEEE*, 8(3), 426-430.
- Lowe, D.G., 2004. Distinctive image features from scale-invariant keypoints. *International journal of computer vision*, 60(2), 91-110.
- Mancini, F., Dubbini, M., Gattelli, M., Stecchi, F., Fabbri, S., and Gabbianelli, G., 2013. Using Unmanned Aerial Vehicles (UAV) for high-resolution reconstruction of topography: The structure from motion approach on coastal environments. *Remote Sensing*, 5(12), 6880-6898.
- McCaffrey, K.J.W., Jones, R.R., Holdsworth, R.E., Wilson, R.W., Clegg, P., Imber, J., Holliman, N., and Trinks, I., 2005. Unlocking the spatial dimension: digital technologies and the future of geoscience fieldwork. *Journal of the Geological Society*, 162(6), 927-938.

- Nouwakpo, S.K., Weltz, M.A., and McGwire, K., 2016. Assessing the performance of structure-from-motion photogrammetry and terrestrial LiDAR for reconstructing soil surface microtopography of naturally vegetated plots. *Earth Surface Processes and Landforms*, 41, 308-322.
- Pearce, M.A., Jones, R.R., Smith, S.A.F., McCaffrey, K.J.W., and Clegg, P., 2006. Numerical analysis of fold curvature using data acquired by high-precision GPS. *Journal of Structural Geology*. 28 1640-1646.
- Pringle, J.K., Clark, J.C., Westerman, A.R., Stanbrook, D.A., Gardiner, A.R., and Morgan, B.E.F., 2001. Virtual outcrops: 3-D reservoir analogues, in *Animations in Geology*, edited by L.Ailleres and T. Rawling, J.Virtual Explorer, 3.
- Pringle, J.K., Westerman, A.R., Clark, J.D., Drinkwater, N.J., and Gardiner, A.R., 2004. 3D high resolution digital models of outcrop analogue study sites to constrain reservoir model uncertainty - Alport Castles, Derbyshire, UK example. *Petroleum Geoscience*. 10, 4, 343-352.
- Pringle, J.K., Howell, J.A., Hodgetts, D., Westerman, A.R., and Hodgson, D.M., 2006. Virtual outcrop models of petroleum reservoir analogues: a review of the current state-of-the-art. *First break*, 24(3).
- Remondino, F., and Fraser, C., 2006. Digital camera calibration methods: considerations and comparisons. *International Archives of Photogrammetry, Remote Sensing and Spatial Information Sciences*, 36(5), 266-272.
- Reshetyuk, Y., 2009. Self-calibration and direct georeferencing in terrestrial laser scanning [PhD thesis]: Stockholm, Sweden. KTH, School of Architecture and the Built Environment (ABE), Transport and Economics, Geodesy.
- Richter, N., Favalli, M., de Zeeuw-van Dalssen, E., Fornaciai, A., da Silva Fernandes, R.M., Rodriguez, N.P., Levy, J., Victória, S.S. and Walter, T.R., 2016. Lava flow hazard at Fogo Volcano, Cape Verde, before and after the 2014-2015 eruption. *Natural Hazards and Earth System Sciences Discussions*.
- Riegl Laser Measurement Systems, 2010, Riegl LMS-Z420i datasheet: [http://www.riegl.com/uploads/tx\\_pxpriegl/downloads/10\\_DataSheet\\_Z420i\\_03-05-2010.pdf](http://www.riegl.com/uploads/tx_pxpriegl/downloads/10_DataSheet_Z420i_03-05-2010.pdf) (04/2016).
- Schober, A., and Exner, U., 2011. 3-D structural modelling of an outcrop-scale fold train using photogrammetry and GPS mapping. *Austrian Journal of Earth Sciences*, 104(2), 73-79.
- Slob, S., and Hack, R., 2004. 3D terrestrial laser scanning as a new field measurement and monitoring technique. In *Engineering Geology for Infrastructure Planning in Europe* (pp. 179-189). Springer Berlin Heidelberg.
- Sturzenegger, M., and Stead, D., 2009. Close-range terrestrial digital photogrammetry and terrestrial laser scanning for discontinuity characterization on rock cuts. *Engineering Geology*, 106(3), 163-182.
- Thurmond, J., Løseth, T., Rivenaes, J., Martinsen, O., Xu, X., Aiken, C., 2006. Using Outcrop Data in the 21st Century – New methods and applications, with example from

- the Ainsa Turbidite System, Ainsa, Spain. In: Nilsen, T., Shew, R., Steffens, G., Studlick, J., Deep-Water Outcrops of the World Atlas. American Association of Petroleum Geologists, Special Publication, CD-ROM.
- Trinks, I., Clegg, P., McCaffrey, K.J.W., Jones, R.R., Hobs, R., Holdsworth, R.E., Holliman, N., Imber, J., Waggott, S., and Wilson, R., 2005. Mapping and analysing virtual outcrops. *Visual Geosciences*, 10(1), 13-19.
- Ullman, S., 1979. The interpretation of structure from motion, *Proc. R. Soc. London, Ser. B*, 203, 405–426.
- Westoby, M.J., Brasington, J., Glasser, N.F., Hambrey, M.J., and Reynolds, J.M., 2012. ‘Structure-from-Motion’ photogrammetry: A low-cost, effective tool for geoscience applications. *Geomorphology*, 179, 300-314.
- Wilkinson, M., McCaffrey, K.J.W., Roberts, G.P., Cowie, P.A., Phillips, R.J., Michetti, A., Vittori, E., Guerrieri, L., Blumetti, A.M., Bubeck, A., Yates, A., and Sileo, G, 2010. Partitioned postseismic deformation associated with the 2009 Mw 6.3 L'Aquila earthquake surface rupture measured using a terrestrial laser scanner. *Geophysical Research Letters*, 37(10).
- Wilkinson, M.W., McCaffrey, K.J., Roberts, G.P., Cowie, P.A., Phillips, R.J., Degasperri, M., Vittori, E., and Michetti, A.M., 2012. Distribution and magnitude of post-seismic deformation of the 2009 L' Aquila earthquake (M6.3) surface rupture measured using repeat terrestrial laser scanning. *Geophysical Journal International*, 189(2), 911-922.
- Wu, C., 2007. SiftGPU: A GPU implementation of Scale Invariant Feature Transform (SIFT). Available from <http://cs.unc.edu/~ccwu/siftgpu>. (Accessed 4<sup>th</sup> August 2016).
- Wu, C., 2013. Towards Linear-time Incremental Structure From Motion. *Proceedings of the 2013 International Conference on 3D Vision*, 127-134, doi 10.1109/3DV.2013.25.
- Wu, C., Agarwal, S., Curless, B., and Seitz, S.M., 2011. Multicore Bundle Adjustment. *Proceedings of the IEEE Computer Society Conference on Computer Vision and Pattern Recognition*, 3057-3064.
- Xu, X., Aiken, C.L., Bhattacharya, J.P., Corbeanu, R.M., Nielsen, K.C., McMechan, G.A., and Abdelsalam, M.G., 2000. Creating virtual 3-D outcrops. *The Leading Edge*, 19(2), 197-202.

## TABLES

TABLE 1. ACQUISITION PARAMETERS, OUTPUT SUMMARY: TERRESTRIAL LASER SCANNING AND STRUCTURE-FROM-MOTION SURVEYS, COMPARISON

	Outcrop 1: Limestone Quarry		Outcrop 2: Ras al-Khaimah
Terrestrial laser scanning (TLS)			
Scanner model	Leica C10		Riegl LMS-Z420i
Step angle (degrees)	0.028		0.032 – 0.040
Distance to outcrop (m)	20 – 50		100 – 200
Theoretical ground sample distance (m)	0.009 – 0.024		0.056 – 0.087
Precision (mm) – $1\sigma$ at 50 m range	6		8
Registration software	Leica Cyclone, version 9.1.4		Riegl RiSCAN PRO, version 1.2.1b9
Average point spacing – point cloud (m)	0.02		0.07
Points in 3D point cloud (million)	1.79		1.40
Point cloud density (pts / m <sup>2</sup> )	1,710		206
Structure-from-motion (SfM) photogrammetry			
Camera body	Nikon D300 12 MP		Canon 650D 18 MP
Pixel size (mm)	0.055		0.043
Lenses	Nikkor 10-24 mm f/3.5-4.5	Nikkor 55-200 mm f4.5-5.6	EF 24-105 mm f/4.0L
Focal length (mm)	24	125	24
Distance to outcrop (m)	10 – 30	200 – 250	60
Images taken	35	165	337
Theoretical ground sample distance – single image pixel spacing (m)	0.004 – 0.011	0.016 – 0.020	0.017
Lens calibration software	Agisoft Lens, version 0.4.1		Agisoft Lens, version 0.4.1
SfM reconstruction software	VisualSFM, version 0.5.26		VisualSFM, version 0.5.26
Average point spacing - point cloud (m)	0.03		0.04
Points in 3D point cloud (million)	0.96		3.36
Point cloud density (pts/m <sup>2</sup> )	880		503
Point-to-point comparison: SfM point cloud relative to the TLS point cloud			
Comparison software	CloudCompare, version 2.7.0		CloudCompare, version 2.7.0
Minimum point-to-point distance (m)	0		0
Maximum point-to-point distance (m)	0.481		0.463
Average point-to-point distance (m)	0.052		0.074
Standard deviation (m, $1\sigma$ )	$\pm 0.048$		$\pm 0.052$
SfM relative precision ratio	1:1563		1:1154

TABLE 2. STRUCTURE-FROM-MOTION PERFORMANCE IN VARIOUS STUDIES

Study author (Type)	Number of images	Range (m)	Compared precision relative to terrestrial laser scanning (m)	Relative precision ratio
Favalli et al., 2012 (outcrops)	4 – 40	$\approx 1$	0.00041 – 0.00376	1:266 – 2439
Favalli et al., 2012 (geological samples)	30 – 67	$\approx 0.3$	0.00023 – 0.00055	1:545 – 1304
James and Robson, 2012 (outcrop)	143	20	0.013 – 0.070	1:286 – 1538
James and Robson, 2012 (geological sample)	92	0.7	0.000133 – 0.00031	1:2258 – 5263
James and Robson, 2012 (airborne and/or large scale)	89	1000	0.56 – 1.00	1:1000 – 1786
Westoby et al., 2012 (outcrop)	889	15	0.1	1:150
Nouwakpo et al., 2016 (outcrop)	25 – 282	2	0.005	1:400
This study (limestone quarry)	200	75	0.048	1:1563
This study (Ras al-Khaimah)	337	60	0.052	1:1154

TABLE 3. PRACTICAL<sup>1</sup> CONSIDERATIONS OF TERRESTRIAL LASER SCANNING (TLS) AND STRUCTURE FROM MOTION (SfM) PHOTOGRAMMETRY FOR DATA ACQUISITION

	TLS	SfM
Typical cost	High (£40k – £150k)	Low (£500 - £8k)
Weight	High (15 – 50 kg)	Low (2 – 15 kg)
Size when packaged for transport	Large (small suitcase sized)	Small (daypack sized)
Number of operators required	1+	1+
Level of operator training	Moderate	Moderate - high
Certainty of success (for critical applications) <sup>2</sup>	High (results available immediately)	Moderate (the final results are only known once the images are processed)
Immediate results in the field	Yes	No
Acquisition time	Comparable with SfM	Comparable with TLS
Precision	High (2 – 8 mm, mostly independent of range)	Ultra high to ultra-low (image resolution and range dependent)
Accuracy	≈5 cm (GPS dependent)	≈5 cm (GPS dependent)
Detail (typical point spacing)	Low-high (range dependent)	Low-high (range dependent)
Internal consistency	High	Moderate
Processing time	Low (minutes to hours)	High (hours to days, dependent on workstation and desired detail)
Additional data	Laser reflection intensity per point	Normal to outcrop surface per point
Versatility in a range of applications <sup>3</sup>	High	Moderate (dependent on operator experience)
Ability to resume survey at a later time	High	Moderate (dependent on similar outcrop appearance)
Multi-day survey, without mains power	Moderate (extra batteries relatively expensive, bulky and heavy)	High (extra batteries relatively cheap, small and light)
Remote operation for temporal survey	Yes	No – operator driven
Automated acquisition <sup>4</sup>	Yes	No – operator driven
Dependence data from other sources	Low (GNSS provides orientation and location)	Moderate (GNSS provides scale, orientation and location)
Depreciation of equipment value	Low	Low-moderate
Ruggedness	Moderate	Moderate
General availability	Low	Moderate-high
Ease of service and availability of replacement parts <sup>5</sup>	Low-moderate	Moderate-high
Equipment used in fieldwork for other purposes?	No	Yes
Ease of transport, import and/or export	Low-moderate	High

<sup>1</sup>For the acquisition of data for rigorous quantitative analysis.

<sup>2</sup>The ability of the operator to review the acquired data in 3D before leaving the field.

<sup>3</sup>To consistently provide quality data for rigorous quantitative analysis.

<sup>4</sup>A measure of how much free time an operator has during the survey for other tasks, such as sample collection.

<sup>5</sup>TLS equipment must usually be returned to the manufacturer for servicing or part replacement by a specialist. SfM uses widely available camera equipment that can be serviced or replaced worldwide. GNSS-Global Navigation Satellite System

TABLE 4. THE RELATIVE PERFORMANCE OF TERRESTRIAL LASER SCANNING (TLS) AND STRUCTURE-FROM-MOTION (SfM) PHOTOGRAMMETRY IN VARIOUS OPERATING CONDITIONS

	TLS	SfM
Rain	Moderate	Low
Fog	Low	Very low
Dust	Moderate	Low
Strong wind	Low	Moderate
Low temperatures (below 0 °C)	Low-moderate	Moderate <sup>1</sup>
High temperatures (above 40 °C)	Moderate	Moderate-high
Direct sunlight on sensor	High	Low
Low light or night time acquisition	High	Low
Very short range (< 1 m)	Low <sup>2</sup>	High
Long range (> 300 m)	High	Low-high <sup>3</sup>
Limited access to the outcrop <sup>4</sup>	Moderate	Low
Temporally changing outcrop appearance during acquisition <sup>5</sup>	High	Very low
Repetitive outcrop with self-similarity	High	Low
Very low contrast outcrop	Moderate-high	Low
Geometrically complex outcrop with limited line of sight	High	Low
Remote outcrops, very rugged terrain	Low	High

<sup>1</sup>SfM camera equipment is perhaps easier to keep warm between uses due to its size.

<sup>2</sup>Based on the majority of TLS units currently on the market which would commonly be used for outcrop acquisition.

<sup>3</sup>Long range performance of SfM is dependent on many factors such as camera resolution, focal length and visibility of the outcrop from a sufficient range of perspectives (which can become increasingly difficult as distance from the outcrop increases).

<sup>4</sup>Situations where the outcrop can only be viewed from a limited number of locations.

<sup>5</sup>Such as extraneous features, lighting, color and reflectivity.

## FIGURES

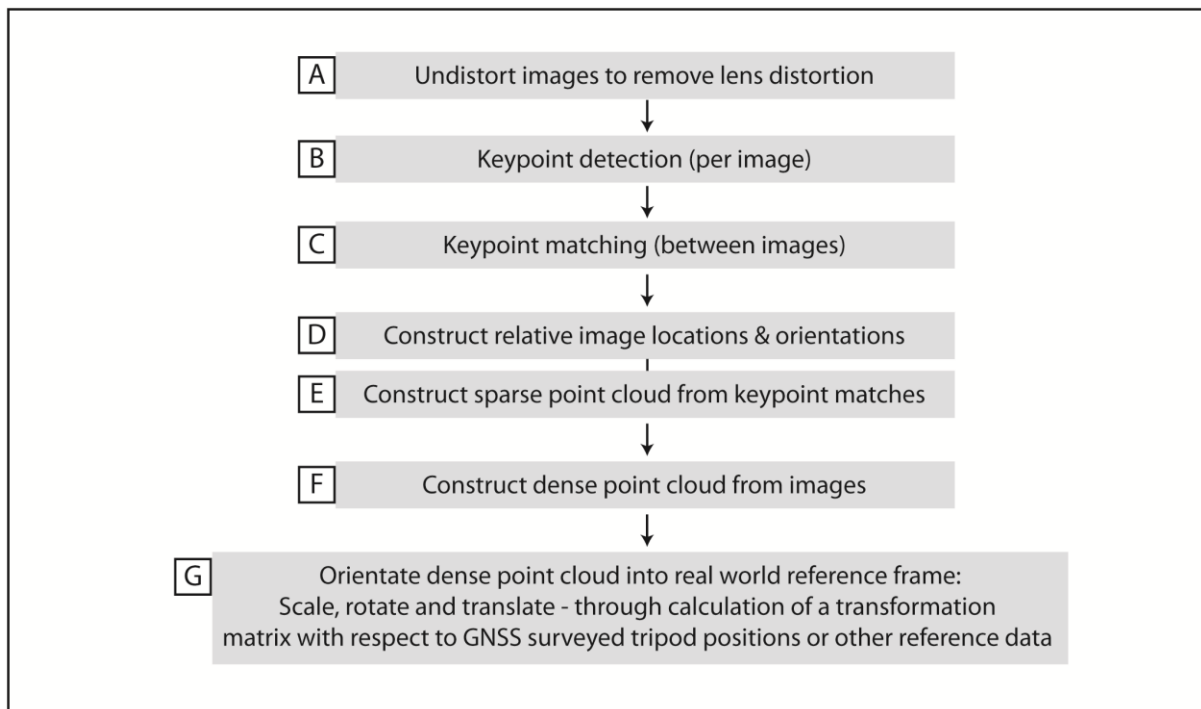


Figure 1. Overview of a typical structure-from-motion (SfM) photogrammetry processing workflow.

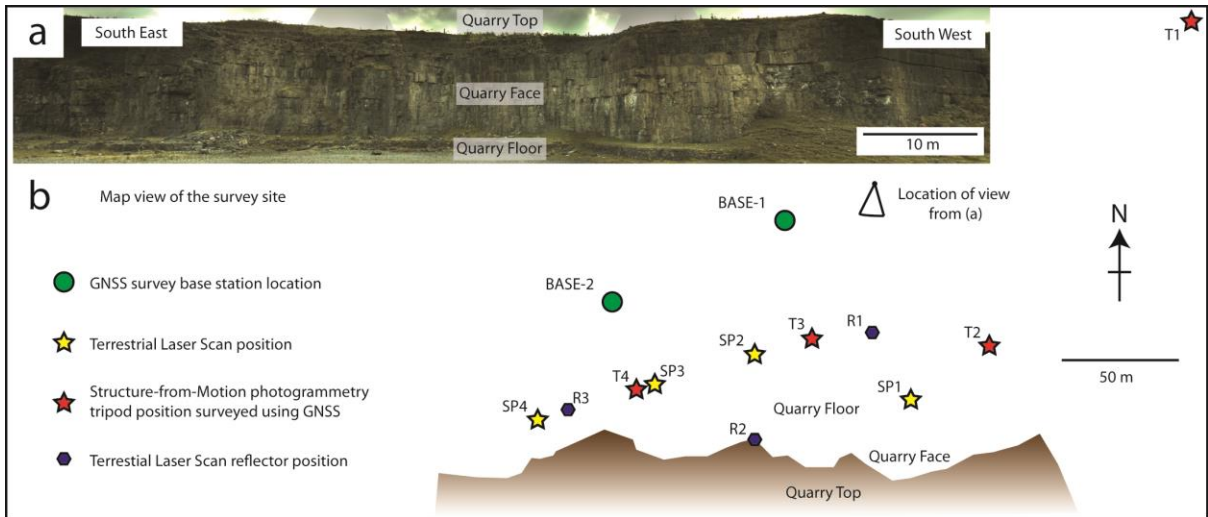


Figure 2. (A) Overview photo of the limestone quarry, looking south. (B) Overview site map.

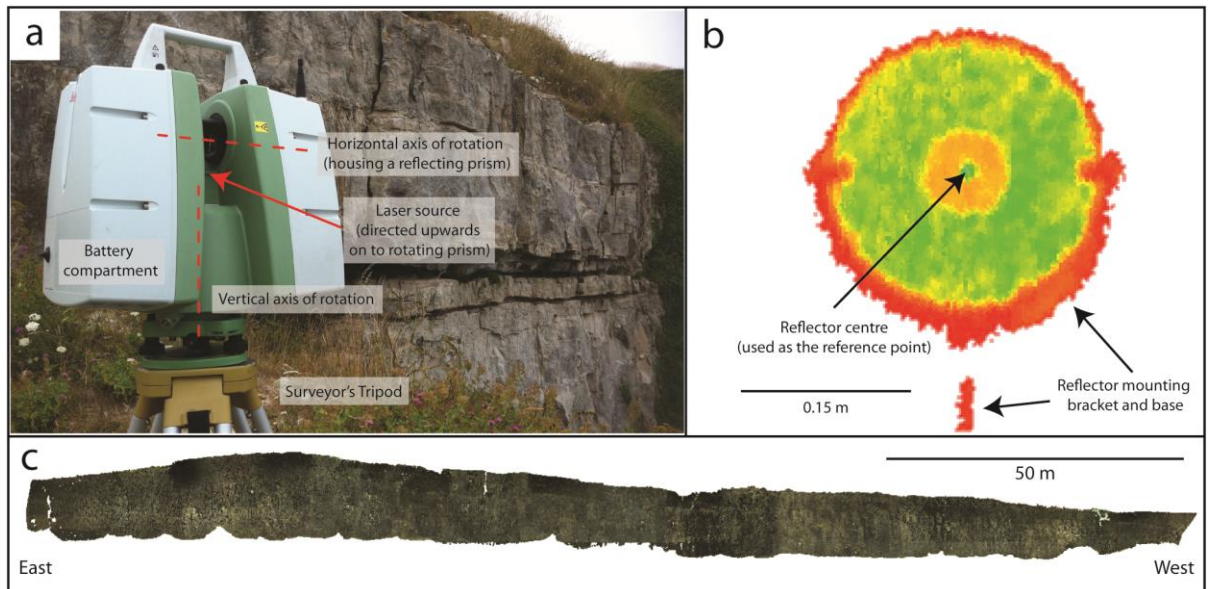


Figure 3. (A) Leica ScanStation C10 laser scanner. (B) Point cloud of one of the retroreflective targets, colored by intensity and used to align the individual scan positions and georeference the final model. (C) The final terrestrial laser scan-derived outcrop model of the quarry.

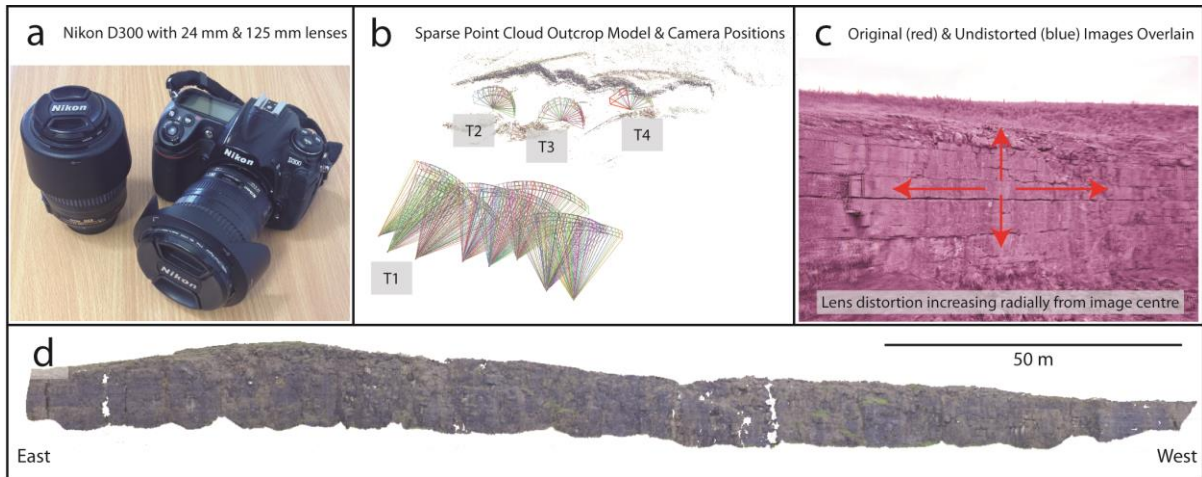


Figure 4. (A) Nikon D300 with zoom lenses taped and calibrated at fixed focal lengths: 24 mm and 125 mm. (B) Sparse point cloud model and camera positions. (C) Comparison of an original image (red) and its undistorted counterpart (blue), overlain. (D) The final structure-from-motion (SfM) photogrammetry-derived outcrop model of the quarry.

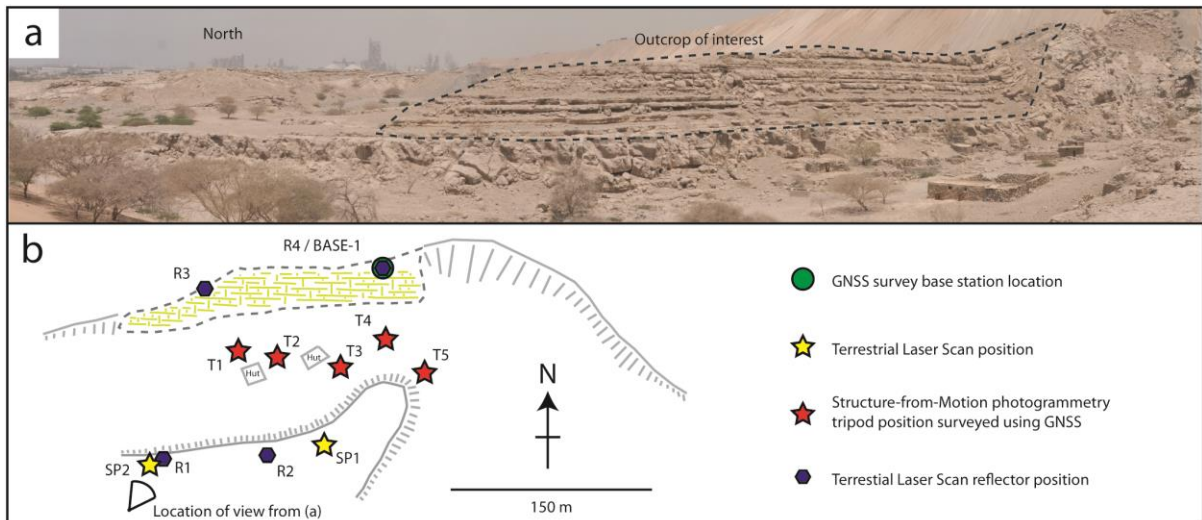


Figure 5. (A) Overview photo of the Ras al-Khaimah outcrop, looking north-northeast. (B) Overview site map.

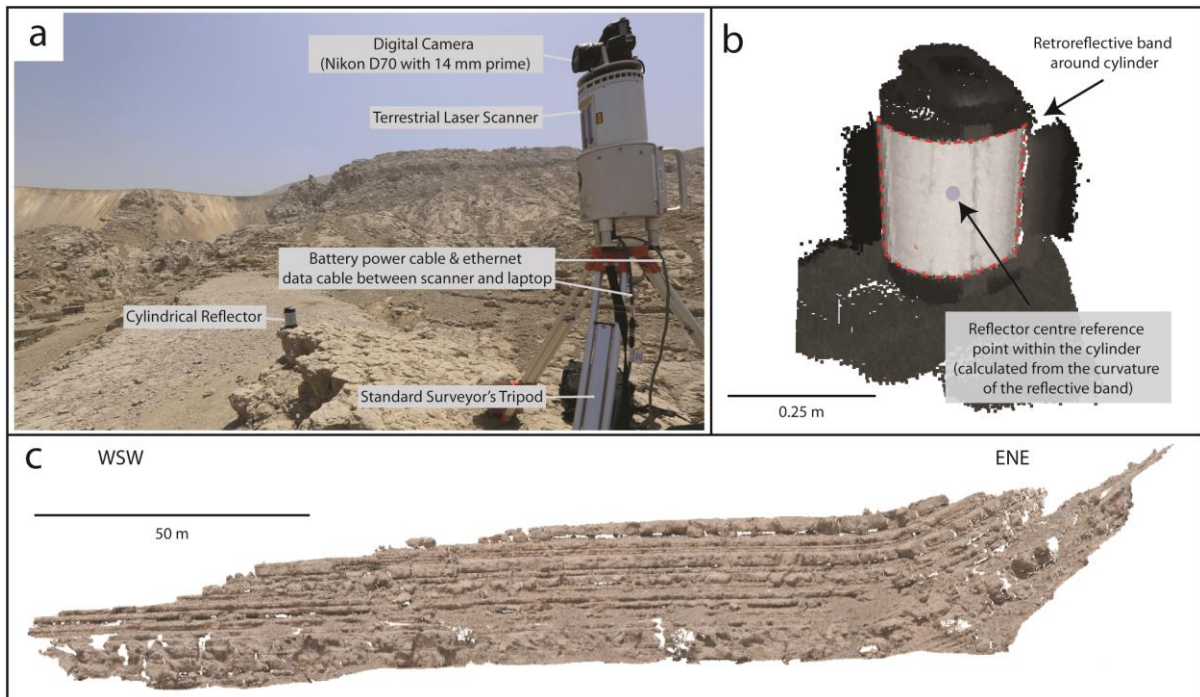


Figure 6. (A) Riegl LMS-Z420i laser scanner. (B) Point cloud of one of the retroreflective cylindrical targets, coloured by intensity and used to align the individual scan positions and georeference the final model. (C) The final terrestrial laser scanning-derived outcrop model.

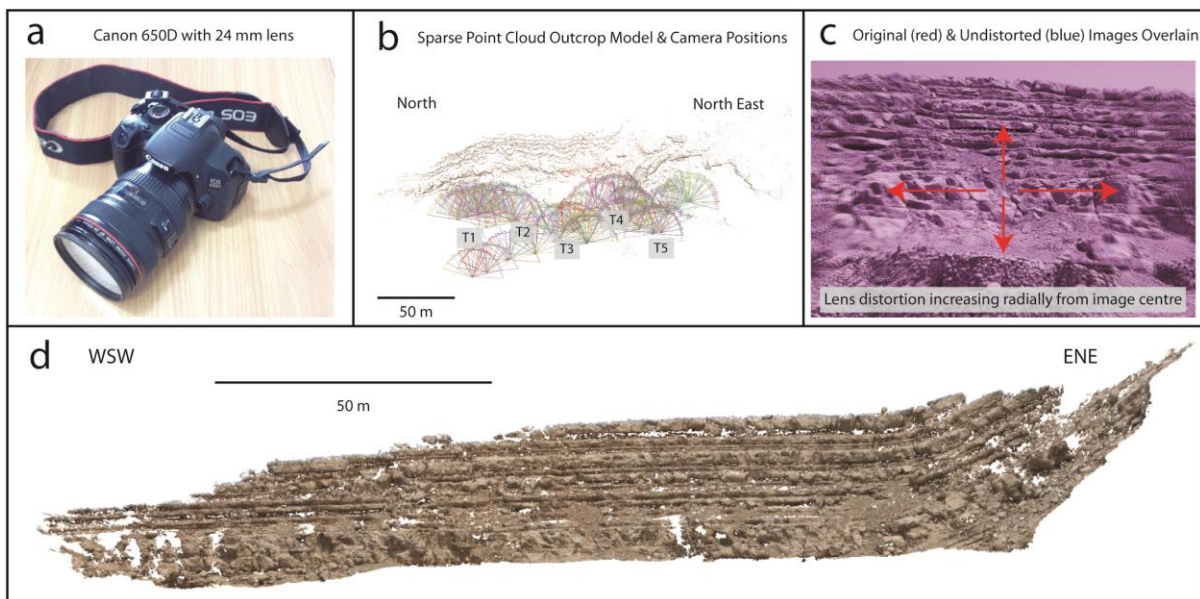


Figure 7. (A) Canon 650D with zoom lens taped and calibrated at 24 mm focal length. (B) Sparse point-cloud model and camera positions. (C) Comparison of an original image (red) and its undistorted counterpart (blue), overlain. (D) The final structure-from-motion (SfM) photogrammetry-derived outcrop model.

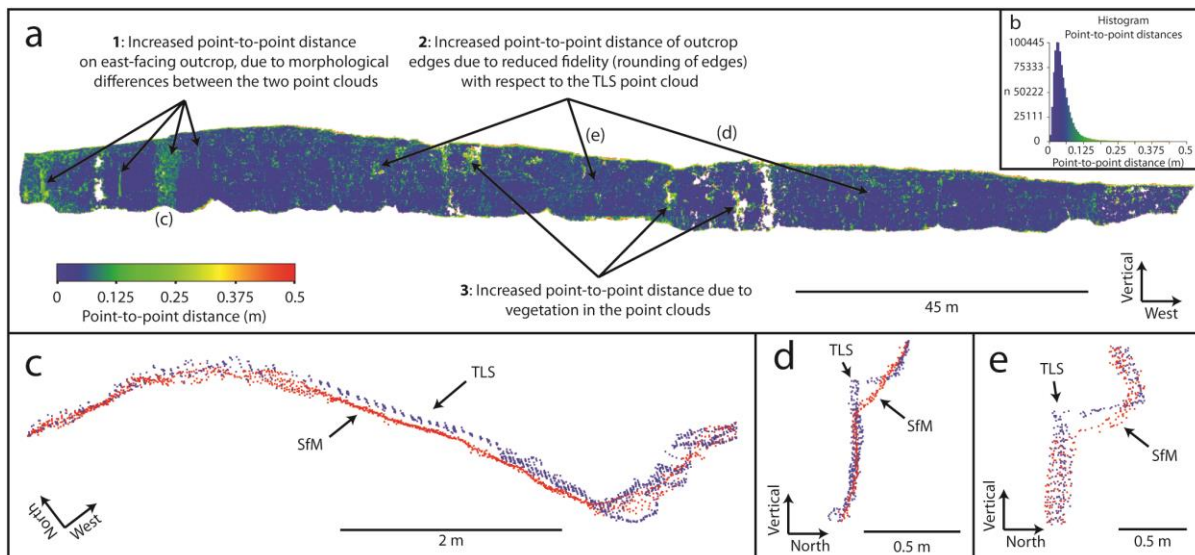


Figure 8. (A) Visualisation of point-to-point distances between terrestrial laser scanning (TLS) and structure-from-motion (SfM) photogrammetry for the limestone quarry data set, showing increased point-to-point distances of three types (1, 2 and 3). (B) Histogram of point-to-point distances. (C) Example offset on east-facing outcrop. (D) and (E) Examples of the rounding off of outcrop edges within the SfM data sets.

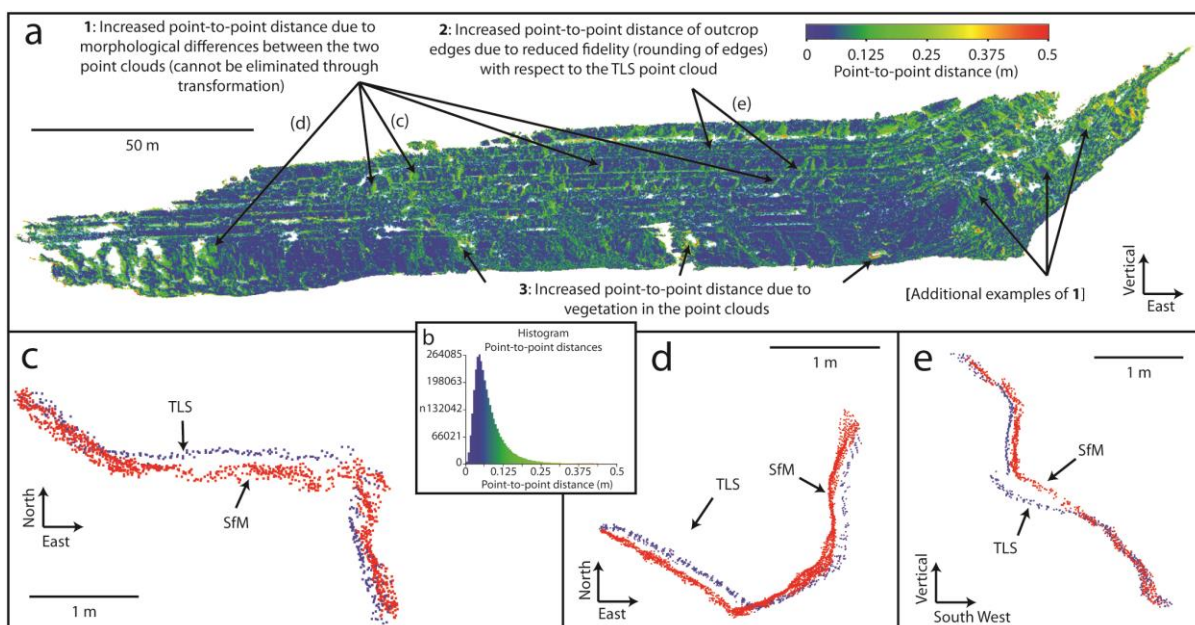


Figure 9. (A) Visualisation of point-to-point distances between terrestrial laser scanning (TLS) and structure-from-motion (SfM) photogrammetry for the Ras al-Khaimah data set, showing increased point-to-point distances of three types: (1, 2 and 3). (B) Histogram of point-to-point distances. (C) and (D) Example offsets due to morphological differences between the two point clouds that cannot be eliminated through homogeneous transformation of the SfM point cloud. (E) Example offset due to rounding off of outcrop edges.

## SUPPLEMENTAL MATERIAL

TABLE S1. REGISTRATION ERRORS BETWEEN TERRESTRIAL LASER SCANNING (TLS) REFLECTIVE TARGETS AND GNSS SURVEYED POSITIONS

Scan position & reflector ID	Error X (m)	Error Y (m)	Error Z (m)	Range error (m)	Mean range error (m)
<b>Limestone Quarry TLS Data set</b>					
SP1 - R1	0.021	0.040	0.013	0.047	0.036
SP1 - R2	0.005	0.007	-0.007	0.011	
SP1 - R3	0.050	-0.026	-0.043	-0.002	
SP2 - R1	0.036	0.022	0.028	0.001	0.035
SP2 - R2	0.010	0.006	0.008	-0.003	
SP2 - R3	0.060	-0.034	-0.050	0.002	
SP3 - R1	0.036	0.022	0.028	0.001	0.035
SP3 - R2	0.014	0.007	0.012	-0.002	
SP3 - R3	0.054	-0.029	-0.049	-0.001	
SP4 - R1	0.034	0.020	0.026	0.007	0.031
SP4 - R2	0.012	0.005	0.011	-0.003	
SP4 - R3	0.047	-0.024	-0.040	-0.003	
<b>Ras al-Khaimah TLS Data set</b>					
SP1 - R1	0.096	-0.040	-0.013	-0.094	0.040
SP1 - R2	-0.017	0.056	0.010	0.053	
SP1 - R3	-0.033	-0.015	0.004	0.036	
SP1 - R4	-0.046	-0.001	-0.001	0.045	
SP2 - R1	-0.001	0.003	0.016	-0.003	0.029
SP2 - R2	0.005	0.011	-0.013	-0.007	
SP2 - R3	-0.048	-0.026	-0.017	0.028	
SP2 - R4	0.044	0.012	0.014	0.011	

TABLE S2. SFM TRANSFORMATION PARAMETERS DESCRIBING THE ALIGNMENT OF THE SFM POINT CLOUD TO THE REAL-WORLD GNSS-DERIVED REFERENCE FRAME AND THE ADDITIONAL FINE-REFINEMENT TO ALIGN THE SFM DATA SET WITH THE TLS DATA SET

Registration type	Transformation parameter	Value
<b>Limestone Quarry SfM Data set</b>		
GNSS-derived registration parameters	Scaling	x 5.460
	Scaling 2 $\sigma$ confidence (95%)	$\pm$ x 0.05
	X-axis rotation	-104.81°
	Y-axis rotation	-6.37°
	Z-axis rotation	164.95°
	RMSE fit to the GNSS data	0.049 m
Fine-refinement transformation to align with the TLS data set	X-axis rotation	-0.21°
	Y-axis rotation	0.00°
	Z-axis rotation	0.11°
	X translation	-0.395 m
	Y translation	-2.896 m
	Z translation	0.096 m
<b>Ras al-Khaimah SfM Data set</b>		
GNSS-derived registration parameters	Scaling	x 8.321
	Scaling 2 $\sigma$ confidence (95%)	$\pm$ x 0.04
	X-axis rotation	-91.87°
	Y-axis rotation	-3.48°
	Z-axis rotation	-2.53°
	RMSE fit to the GNSS data	0.062 m
Fine-refinement transformation to align with the TLS data set	X-axis rotation	-0.24°
	Y-axis rotation	-0.01°
	Z-axis rotation	0.21°
	X translation	0.586 m
	Y translation	-0.629 m
	Z translation	0.858 m

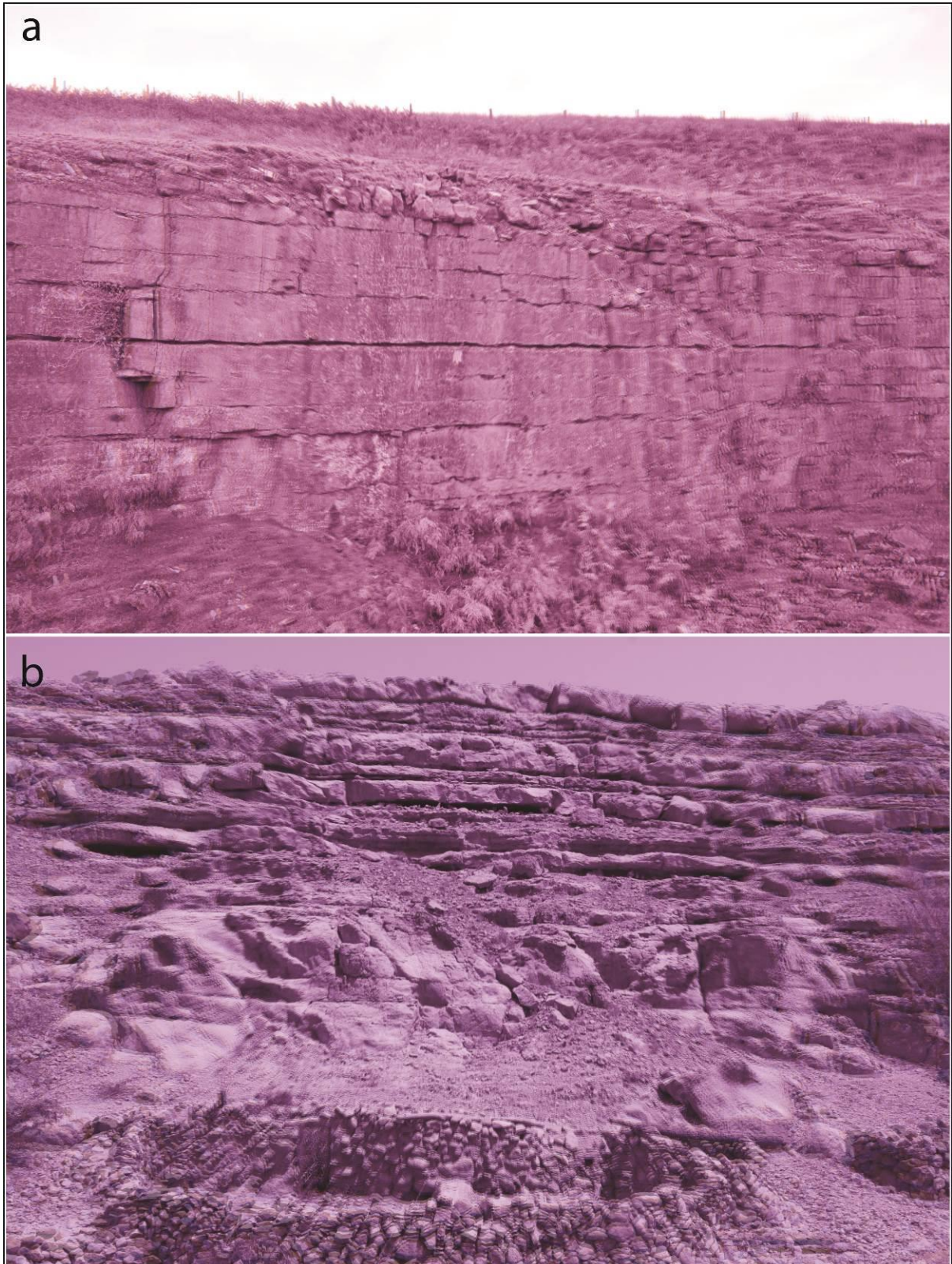


Figure S1: High resolution versions of (A) figure 4C, and (B) figure 7C.